

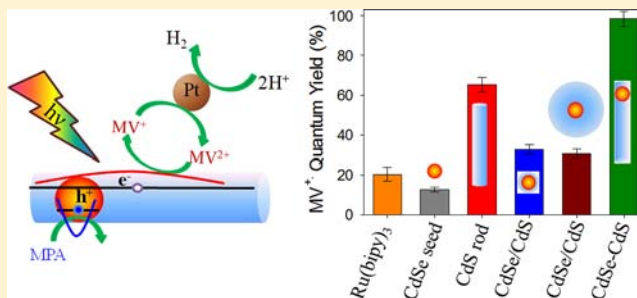
Near Unity Quantum Yield of Light-Driven Redox Mediator Reduction and Efficient H₂ Generation Using Colloidal Nanorod Heterostructures

Haiming Zhu, Nianhui Song, Hongjin Lv, Craig L. Hill, and Tianquan Lian*

Department of Chemistry, Emory University, Atlanta, Georgia 30322, United States

S Supporting Information

ABSTRACT: The advancement of direct solar-to-fuel conversion technologies requires the development of efficient catalysts as well as efficient materials and novel approaches for light harvesting and charge separation. We report a novel system for unprecedentedly efficient (with near-unity quantum yield) light-driven reduction of methylviologen (MV²⁺), a common redox mediator, using colloidal quasi-type II CdSe/CdS dot-in-rod nanorods as a light absorber and charge separator and mercaptopropionic acid as a sacrificial electron donor. In the presence of Pt nanoparticles, this system can efficiently convert sunlight into H₂, providing a versatile redox mediator-based approach for solar-to-fuel conversion. Compared to related CdSe seed and CdSe/CdS core/shell quantum dots and CdS nanorods, the quantum yields are significantly higher in the CdSe/CdS dot-in-rod structures. Comparison of charge separation, recombination and hole filling rates in these complexes showed that the dot-in-rod structure enables ultrafast electron transfer to methylviologen, fast hole removal by sacrificial electron donor and slow charge recombination, leading to the high quantum yield for MV²⁺ photoreduction. Our finding demonstrates that by controlling the composition, size and shape of quantum-confined nanoheterostructures, the electron and hole wave functions can be tailored to produce efficient light harvesting and charge separation materials.



INTRODUCTION

Direct solar-to-fuel conversion has been intensely investigated in recent years as a potential approach for solar energy conversion and storage.¹ The overall process consists of two half reactions: the oxidation of water to O₂ (2H₂O → 2O₂ + 4H⁺ + 4e⁻) and the reduction of CO₂ or water (2H⁺ + 2e⁻ → 2H₂) to form fuel. A general photoreduction scheme, depicted in Figure 1A, involves (i) the absorption of light by the sensitizer (with efficiency ϕ_{LH}), (ii) the charge separation and reduction of the catalyst by direct electron transfer or via redox mediators (with efficiency ϕ_{col}), and (iii) the turnover of the substrates to fuel by the reduced catalyst (with efficiency ϕ_{cat}). The efficiencies of these processes determine the overall external quantum efficiency of solar-to-fuel conversion, defined as the ratio of products to incident photons, $\Phi = \phi_{LH} \times \phi_{col} \times \phi_{cat}$. Therefore, the advancement of solar-to-fuel conversion technologies requires the development of efficient catalysts (increasing ϕ_{cat}) for H₂ evolution and CO₂ reduction as well as better materials and approaches for light harvesting and charge separation (increasing ϕ_{LH} , ϕ_{col}).

Quantum-confined semiconductor nanocrystals (NCs) have many characteristics that are ideal for light-harvesting and charge separation applications.²⁻⁴ Compared to molecular chromophores,⁵⁻⁸ these NCs offer unique size-dependent absorption properties, large extinction coefficients over a broad spectral range, long exciton lifetimes, the possibility of

generating multiple excitons by single photons, and enhanced photostability.^{3,4,9} The surface of NCs can be readily modified for specific functional targets and/or reaction environments.¹⁰⁻¹² Recent advances in the synthesis of nanoheterostructures consisting of two or more materials provide additional control of the electron and hole wave functions in these materials (i.e., wave function engineering) for optimizing charge separation and photocatalytic properties.^{4,13-16} Furthermore, some of these nanoheterostructures have built-in directional charge separation and catalytic units,^{17,18} resembling the well-studied molecular dyads and triads.¹⁹⁻²¹

Many solar-to-fuel conversion processes, such as H₂ evolution or CO₂ reduction, require the transfer of multiple electrons. Because a single photon absorption event results in the excitation and transfer of one electron in most light-harvesting materials, effective schemes for accumulating multiple electrons at the catalyst while simultaneously suppressing charge recombination processes are also required. In nature, one-electron redox mediators/relays can be used to sequentially deliver the electrons from the light-harvesting units to the catalytic centers.²² It has been reported that MV^{2+/•+} couple (-0.45 vs NHE in aqueous solution) can act as an effective one-electron mediator for multielectron photocatalytic

Received: April 17, 2012

Published: June 21, 2012

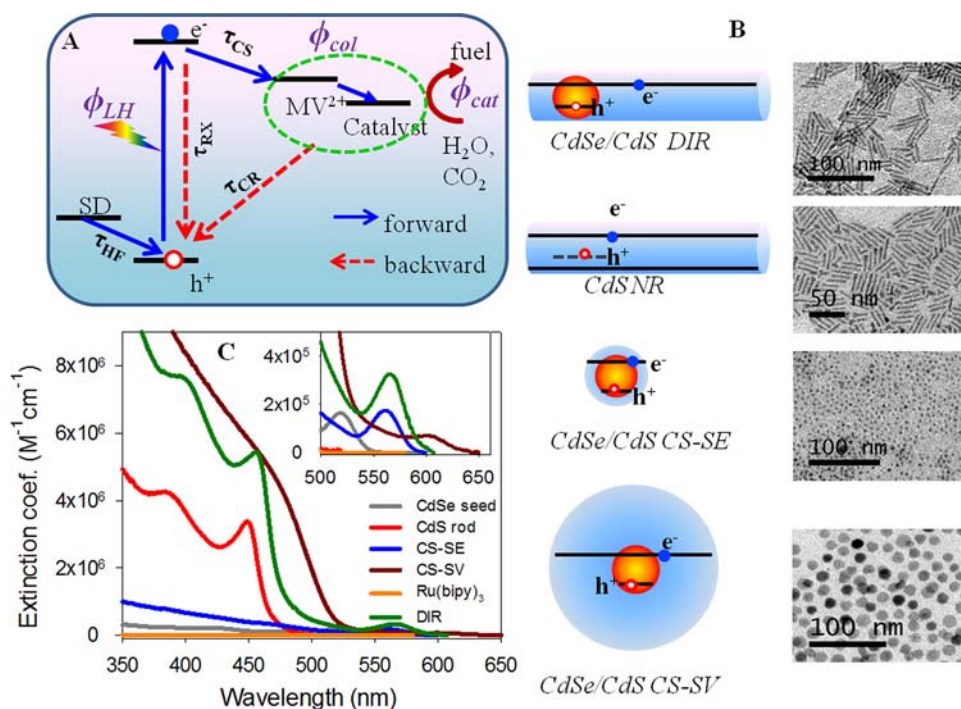


Figure 1. (A) Schematic depiction of relevant processes in a solar-to-fuel conversion system containing sacrificial electron donor (SD), sensitizer, redox mediator (methylviologen, MV^{2+}), and catalyst. The competitions between the forward reactions (electron transfer and hole filling, with time constant τ_{CS} and τ_{HF} , respectively) and backward reactions (exciton and charge recombination, with time constants τ_{RX} and τ_{CR} , respectively) determine the charge collection efficiency (ϕ_{col}). (B) Schematic structures (left) and TEM images (right) of CdSe/CdS dot-in-rod (DIR) nanorods (NRs) as well as CdS NRs of similar dimensions, CdSe/CdS core/shell QDs of similar lowest exciton energy (CS-SE), and CdSe/CdS core/shell QDs of similar volume (CS-SV) as the DIR. The horizontal lines in the schematic structures indicate the extent of delocalization of the lowest energy conduction band electron and valence band hole. (C) Extinction coefficient spectra of CdSe/CdS DIR, CdSe seed, CdS NR, CdSe/CdS CS-SE, CdSe/CdS CS-SV, and $Ru(bipy)_3^{2+}$. (Inset) Expanded view of the lowest energy exciton bands.

reactions, such as H_2 evolution (with $Pt^{5,23,24}$ and hydrogenase^{25,26}), CO_2 reduction (with formate dehydrogenase²⁷ and Pd^{28}) and other reductase-dependent reactions.^{29–32} Thus, efficient solar-to-fuel conversion can be realized if a scheme for efficient light-driven photoreduction of MV^{2+} or other redox mediators can be developed. Although electron transfer from semiconductor NCs to MV^{2+} has been observed,^{33,34} charge recombination is also rapid in NC– MV^{2+} complexes (see below). As a result, an efficient system for photogeneration of $MV^{+•}$ radicals and photocatalysis has yet to be developed.^{35,36}

Herein, we report a colloidal quasi-type II^{16,37} nanorod (NR)-based system for the photogeneration of $MV^{+•}$ radicals with near-unity quantum efficiency over a broad MV^{2+} concentration range (0.040–125 mM). The system consists of a simple mixture of 3-mercaptopropionic acid (MPA)-capped water-soluble CdSe/CdS dot-in-rod (DIR) NRs, MV^{2+} , and excess MPA in aqueous solution. Addition of Pt nanoparticles (NPs) into the above system leads to direct conversion of solar energy to H_2 with a ~14% internal quantum efficiency, demonstrating the applicability of this highly efficient and flexible $MV^{+•}$ radical generation system for solar-to-fuel conversion. To understand the origin of the unprecedented high steady-state MV^{2+} photoreduction efficiency, we compare the quantum efficiencies and transient kinetics of the CdSe/CdS DIR with a commonly used molecular chromophore, $Ru(bipy)_3^{2+}$, and related nanostructures of different shapes and dimensions (Figure 1B). These NCs include CdSe seed quantum dots (QDs) used to prepare the DIR, CdS NRs of similar dimensions (diameter and length), CdSe/CdS core/shell QDs of similar lowest exciton energy (CS-SE), and giant

CdSe/CdS core/shell QDs of similar volume (CS-SV). These comparisons show that the electron and hole wave functions in the CdSe/CdS quasi-type II DIR enable ultrafast electron transfer to MV^{2+} , ultrafast hole filling by MPA, and ultraslow charge recombination, resulting in the near-unity quantum yield of $MV^{+•}$ radical generation. Our study demonstrates the possibility of using wave function engineering to enhance light-harvesting and charge separation properties of quantum confined nanoheterostructures.

RESULTS AND DISCUSSIONS

MV^{2+} photoreduction. The CdSe/CdS DIR, CdSe/CdS CS-SE, and CdSe/CdS CS-SV heterostructures used in this study are grown from the same CdSe seed QDs. The synthesis procedures and size distributions of the CdSe seed QDs, CdSe/CdS heterostructures, and CdS NRs are described in the Supporting Information (SI). CdSe/CdS DIR was synthesized via a seeded-growth method in trioctylphosphine oxide (TOPO).³⁸ Starting from TOPO-capped CdSe seed with a lowest exciton peak at 520 nm (2.6 nm in diameter³⁹), TOPO-capped CdSe/CdS DIR of 3.1 ± 0.2 nm in diameter and 35.3 ± 2.3 nm in length (Figure 2B and Figure S1 in SI) was prepared. After ligand exchange, mercaptopropionic acid (MPA)-capped water-soluble NRs were obtained. It should be noted that CdS NR, CdSe/CdS DIR, and CdSe/CdS CS-SV have similar volumes and surface areas (within a factor of 2–3). The extinction coefficient (EC) spectra of CdSe seed, CdS rod, CdSe/CdS DIR, CdSe/CdS CS-SE, CdSe/CdS CS-SV, and $Ru(bipy)_3^{2+}$ are compared in Figure 2A. The EC spectra of CdSe seed and $Ru(bipy)_3^{2+}$ are deduced from literature

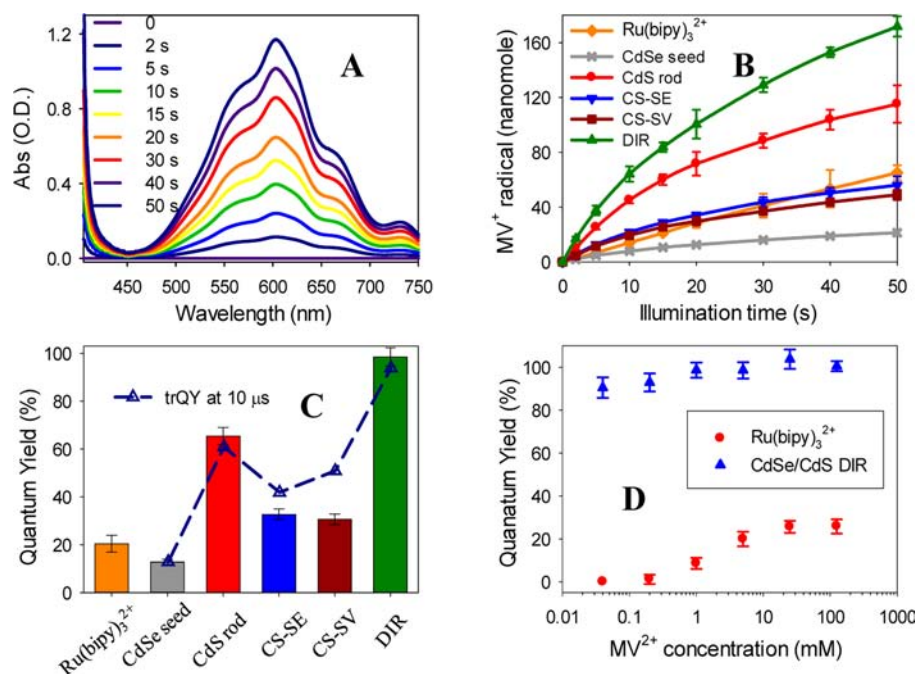


Figure 2. Steady-state photoreduction of MV^{2+} . (A) UV–vis difference spectra (after–before irradiation) of a solution containing CdSe/CdS DIR, MV^{2+} and MPA after indicated time of irradiation, showing the generation of MV^{\bullet} radicals. Similar spectra using other NCs are shown in Figure S3 of SI. Experimental conditions: light source (wavelength 455 nm, power 2.4 mW, beam diameter at sample ~ 0.4 cm), absorbance of sensitizers at 455 nm (1.1 OD), sacrificial electron donor (50 mM MPA for NCs and 50 mM TEOA for $Ru(bipy)_3^{2+}$), 5 mM MV^{2+} , 50 mM pH 7.8 phosphate buffer, total reaction volume (2 mL). (B) MV^{\bullet} radical generation kinetics using different sensitizers. (C) Initial quantum yields of MV^{\bullet} radical generation using different sensitizers (bars). Also plotted are the transient quantum yields (open triangles) at 10 μs obtained from transient absorption measurements. (D) Dependence of the initial quantum yield on MV^{2+} concentration (0.040–125 mM) for $Ru(bipy)_3^{2+}$ and CdSe/CdS DIR.

Table 1. Measured and Estimated Time Constants and Yields for Processes Shown in Figure 1: Charge Separation (τ_{CS}), Intrinsic Exciton Recombination (τ_{RX}), Charge Recombination (τ_{CR}), Hole Filling (τ_{HF}), Steady-State MV^{\bullet} Radical Generation Yield (Φ_{MV}), and Transient Quantum Yield at 9–10 μs (Φ_{TA}) (TA = transient absorption)

| Sensitizer type | τ_{CS} (ps) | τ_{RX} (ps) | τ_{CR} (ns) | τ_{HF} (ns) | Φ_{TA} (%) | Φ_{MV} (%) |
|-----------------|------------------|------------------|------------------|------------------|-----------------|-----------------|
| CdSe seed | 0.4 | > 1000 | 0.14 | 0.15 | 13 | 11.4 \pm 1.3 |
| CdS NR | 0.5 | | 20 | 0.62 | 61 | 65.3 \pm 3.6 |
| CdSe/CdS CS-SE | 0.4 | | 4 | 0.36 | 42 | 32.6 \pm 2.3 |
| CdSe/CdS CS-SV | 20 | | 2250 | \gg 100 | 51 | 30.6 \pm 4.2 |
| CdSe/CdS DIR | 0.4 | | 320 | 0.31 | 94 | 98.2 \pm 3.8 |

values,^{6,39} and the EC spectra of all other NCs are estimated from their UV–vis absorption spectra by assuming that their concentrations are the same as those of the CdSe seed used to start the growth process. Because of the loss of NCs in the synthesis and purification process, the estimated ECs should be considered as a lower limit with $\sim 20\%$ error. All semiconductor NCs have much higher ECs over a broader spectral range than $Ru(bipy)_3^{2+}$. CdSe/CdS heterostructures exhibit the absorption properties of both the CdSe seed and CdS shell or rod, as well as new CdSe-to-CdS transitions, thus exhibiting improved light-harvesting ability compared to single-component nanomaterials (CdSe seed or CdS rod).

Photoreduction of MV^{2+} was performed by mixing sensitizers, MV^{2+} (5.0 mM) and sacrificial electron donors in anaerobic pH = 7.8 aqueous solutions where all NCs were well dissolved to form a homogeneous system (SI). Excess (50 mM)

MPA and triethanolamine (TEOA) were used as sacrificial electron donors for NCs and $Ru(bipy)_3^{2+}$, respectively. The sensitizer (MPA-capped NC or $Ru(bipy)_3^{2+}$) concentrations were adjusted to ensure that all solutions had the same absorbance at the illumination wavelength (1.1 OD at 455 nm). Under these conditions, the CdSe/CdS DIR concentration ($\sim 0.2 \mu M$) was ~ 500 -fold smaller than that of $Ru(bipy)_3^{2+}$. Upon illumination of a solution containing CdSe/CdS DIR, MV^{\bullet} radicals formed quickly, as indicated by the growth of a distinct 605 nm band in the difference spectra shown in Figure 2A. This feature can be attributed to MV^{\bullet} radicals because MPA and MV^{2+} have negligible absorption in this spectral range. Complete sets of steady state UV–vis difference spectra for all sensitizers are shown in Figure S3 of SI. In the absence of sensitizers or illumination, no MV^{\bullet} radicals were observed, indicating that these reactions are indeed photodriven. Using

the reported extinction coefficient ($13700 \pm 300 \text{ M}^{-1} \text{ cm}^{-1}$ at 605 nm),⁴⁰ the amount of $MV^{+\bullet}$ radicals can be calculated to obtain the radical formation kinetics, which are shown in Figure 2B.

To quantify the performance of these sensitizers, we compare their photon-to- $MV^{+\bullet}$ conversion quantum yields defined as $\Phi_{MV} = \Delta(MV^{+\bullet})/\Delta(h\nu)$, where $\Delta(MV^{+\bullet})$ is the $MV^{+\bullet}$ generation rate and $\Delta(h\nu)$ is the photon absorption rate of the reaction solution, respectively. The latter can be calculated from the illumination light intensity and UV–vis absorption spectrum (see SI for details) and is the same for all samples. The $MV^{+\bullet}$ generation rate is the slope of $MV^{+\bullet}$ -vs-time plots shown in Figure 2B. It is the largest at the beginning of the reaction and decreases slowly with time due to the consumption of the electron and/or hole acceptors. For this reason, only the initial quantum yields, calculated from the initial $MV^{+\bullet}$ generation rate (0–5 s), for different sensitizers are compared in Figure 2C and Table 1.

Under our experimental conditions, $\text{Ru}(\text{bipy})_3^{2+}$ shows a $20.4 \pm 3.5\%$ initial quantum yield for $MV^{+\bullet}$ radical generation, in agreement with the reported values for the same sensitizer under similar conditions.^{41–43} The initial quantum yield for the CdSe seed is relatively low ($11.4 \pm 1.3\%$). However, for CdSe/CdS DIR, the yield increases by 1 order of magnitude to near-unity ($98.2 \pm 3.8\%$), indicating that nearly every absorbed photon leads to the reduction of one MV^{2+} molecule with negligible loss. The initial quantum yields for other sensitizers (CdS NR, CdSe/CdS CS-SE, and CdSe/CdS CS-SV) fall between the values of CdSe seed and CdSe/CdS DIR.

The quantum yields reported above were measured in solutions with 5 mM MV^{2+} . Under these conditions, less than 2% of the MV^{2+} was reduced after 50 s of illumination. It has been pointed out that as an electron mediator, a high concentration of MV^{2+} is undesirable in some photocatalytic systems because of either reversed transformation of the product to reactant, such as $MV^{2+} + 1/2H_2 + OH^- \xrightarrow{Pt} MV^{+\bullet} + H_2O$ or the adsorption of MV^{2+} on catalysts, blocking the active sites.^{44–46} We compare the initial quantum yields of MV^{2+} photoreduction as a function of MV^{2+} concentration for $\text{Ru}(\text{bipy})_3^{2+}$ and CdSe/CdS DIR in Figure 2D. In this experiment, the MV^{2+} concentration was varied between 40 μM and 125 mM, while other experimental conditions remained the same as those used in Figure 2A. The kinetics for $MV^{+\bullet}$ radical formation at all MV^{2+} concentrations can be found in SI. For $\text{Ru}(\text{bipy})_3^{2+}$, the initial quantum yield is strongly dependent on MV^{2+} concentration, which is $<0.1\%$ (below the detection limit) at 40 μM and saturates at $26 \pm 3\%$ at 25 mM. This is consistent with the expected bimolecular quenching between the excited $\text{Ru}(\text{bipy})_3^{2+}$ and MV^{2+} , whose quantum yield decreases at lower MV^{2+} concentrations.⁴³ Therefore, undesirably high MV^{2+} concentrations are sometimes used in catalytic systems employing $\text{Ru}(\text{bipy})_3^{2+}$ sensitizers.^{45,47} For CdSe/CdS DIR, the quantum yield remains high ($>90\%$) over the evaluated concentration range (0.040–125 mM). The weaker MV^{2+} concentration dependence indicates the formation of NC– MV^{2+} complexes, likely facilitated by the electrostatic interaction between the MV^{2+} cations and the negatively charged NCs or surface sites. The presence of NC– MV^{2+} complexes is further confirmed by the observation of ultrafast electron transfer from excited NCs to MV^{2+} , which will be discussed below. Thus, the easily controlled surface properties of NCs enable the formation of

sensitizer/quencher complexes through electrostatic interaction, providing a simple method for constructing efficient redox mediator photoreduction systems.

H_2 Evolution Coupled with Pt As Catalyst. $MV^{+\bullet}$ radicals are known to drive water or CO_2 reduction in the presence of catalysts.^{2,21,27} To demonstrate the utility of the NC-based MV^{2+} photoreduction systems for solar-to-fuel conversion applications, we added colloidal Pt nanoparticles (0.8 mM, capped by polyvinyl alcohol), which is dispersed in the solution, as the catalyst for H_2 generation. The NC, MPA, and MV^{2+} concentrations are the same as those reported in Figure 2A. It has been reported that efficient H_2 evolution using $MV^{+\bullet}$ radicals and colloidal Pt catalysts requires acidic pH conditions and, indeed, we did not observe significant H_2 generation under pH = 7.8. Therefore, a pH = 6.2 phosphate buffer was used here to increase the H_2 generation rate.⁴⁴ Because of the protonation of MPA (the thiol group) at the acidic conditions, the ligand partially dissociated from the NC surface and led to the precipitation of some NCs.⁴⁸ To overcome this problem, the hydrogen evolution experiment was performed under rigorous stirring, which generated a NC suspension. Upon illumination, the amount of photogenerated H_2 increases linearly with time in the experimental period (40 min) for all sensitizers (Figure 3A). Control experiments show

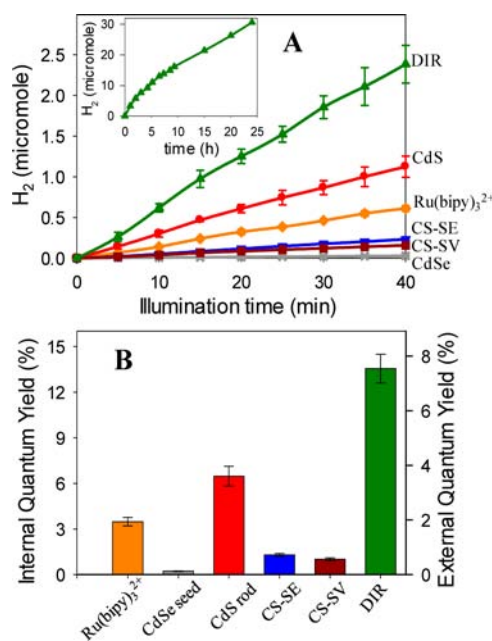


Figure 3. (A) Kinetics of H_2 formation from water reduction using different sensitizers in the first 40 min. (Inset) the H_2 formation kinetics using CdSe/CdS DIR up to 24 h. Conditions: MV^{2+} , MPA, and NCs concentrations (same as stated in Figure 2A caption); 50 mM, pH = 6.2 phosphate buffer; H_2 evolution catalyst (0.8 mM Pt nanoparticles); and illumination light (8 mW, 455 nm). (B) Internal (left axis) and external (right axis) quantum yields of H_2 evolution using different sensitizers.

that all three components, MV^{2+} , Pt, and light illumination, are necessary for H_2 generation. The quantum yield of H_2 generation can be calculated by $\Phi_{H_2} = 2\Delta(H_2)/\Delta(h\nu)$ where $\Delta(H_2)$ is the H_2 generation rate, and the factor of 2 accounts for the requirement of two electrons per H_2 molecule. An external quantum yield of $7.5 \pm 0.6\%$ is obtained for CdSe/CdS DIR. After correction for Pt absorption and cell reflection, an

internal quantum yield of $13.6 \pm 1.0\%$ was estimated for CdSe/CdS DIR (see SI for details). These internal and external quantum yields are compared in Figure 3B for different sensitizers. The values for internal quantum yields represent a lower limit because the scattering loss of the suspension has not been taken into account. The trend of H_2 -generation efficiencies agrees well with that of MV^{2+} radical generation efficiencies, suggesting that the modest overall H_2 generation quantum efficiencies are limited mainly by the low catalytic efficiency of the Pt NPs used in this study. The efficiency can be improved with the optimization of the experimental conditions and the use of more efficient H_2 evolution catalysts (e.g., hydrogenase). The H_2 turnover number for each CdSe/CdS nanorod reaches 82500 during a 24 h test period without significant loss of activity (Figure 3A inset), indicating the stability and applicability of the DIR-based MV^{2+} photo-generation system for solar-to-fuels conversion.

Mechanism for Efficient MV^{2+} Photoreduction. As illustrated in Figure 1A, the overall MV^{2+} radical generation quantum yield depends on the rates of charge separation, charge recombination, and hole-filling processes in the system. To understand the origin of the different MV^{2+} photoreduction performances for the nanostructures discussed above, we used time-resolved transient absorption and fluorescence decay spectroscopy to directly measure the rates of these steps. We first conducted transient absorption measurements on the complete photoreduction systems under conditions similar to those for the steady-state MV^{2+} photoreduction described in Figure 2A (see SI for details). The NC concentrations have been increased by ~ 4 times to allow measurement in a thinner cell needed to maintain ultrafast time resolution (~ 150 fs). The transient spectra and exciton bleach recovery kinetics of samples with and without MV^{2+} are compared in Figure S5 in SI. In the absence of MV^{2+} , the lowest energy exciton bleach is long lived, indicating long-lived conduction band electrons in these NCs. In the presence of MV^{2+} , the transient bleach of the exciton band undergoes fast and complete recovery (Figure S5 in SI). After the bleach recovery, the TA spectra consist of derivative-like features of the exciton bands and the broad absorption of MV^{2+} radicals centered at 605 nm. The former can be attributed to the Stark-effect induced exciton peak-shift of the NC- MV^{2+} complexes in the charge separated state ($\text{NC}^+-\text{MV}^{2+}$).^{13,14} The formation of these spectral features and the recovery of exciton bleach confirm the transfer of electrons from NCs to MV^{2+} .

The kinetics of the formation and decay of MV^{2+} radicals can be monitored at 605 nm (650 nm for CdSe/CdS CS-SV), where NCs have negligible absorption as shown in Figure S5 in SI. The normalized MV^{2+} radical kinetics for all NCs are compared in Figure 4A, from which we determined the half-life time for MV^{2+} radical formation to represent the effective charge separation time (τ_{CS} in Table 1). The electron transfer times from all NCs to MV^{2+} are ultrafast (~ 0.4 – 0.5 ps) except for CdSe/CdS CS-SV (~ 20 ps). These rates are similar to those measured in QD- MV^{2+} complexes formed in organic solvents (Figure S6 in SI)³⁴ and significantly faster than the diffusion-limited bimolecular quenching rate (estimated to be $5 \times 10^6 \text{ s}^{-1}$ from the reported rate constant of $\sim 10^9 \text{ M}^{-1} \text{ s}^{-1}$ and MV^{2+} concentration of 5 mM).⁴¹ These ultrafast electron transfer rates and the negligible concentration-dependent radical formation quantum yields discussed above suggest that electron transfer occurs within the NC- MV^{2+} complexes formed in aqueous solutions.

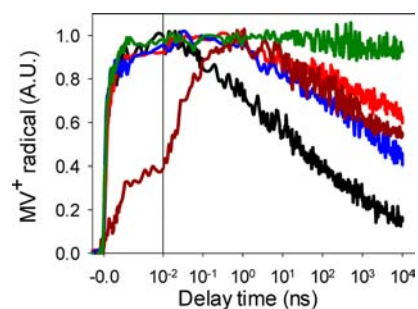


Figure 4. Comparison of the formation and decay kinetics of MV^{2+} radicals generated by 400 nm excitation of aqueous solutions containing different NCs: CdSe seed (black), CdSe/CdS CS-SE (blue), CdSe/CdS CS-SV (dark red), CdS rod (red), and CdSe/CdS DIR (green). The amplitude represents the transient quantum yield of MV^{2+} radicals (see main text for details). The x -axis is in linear scale from -2 to 10 ps and in logarithmic scale from 10 ps to $10 \mu\text{s}$.

The ultrafast and complete bleach recovery and ultrafast MV^{2+} radical formation (Figure 4 and S5 in SI) suggests that the initial charge separation yield is 100% in all NC- MV^{2+} complexes. Therefore, the amplitude of the normalized kinetics in Figure 4 represents the transient quantum yield, $\Phi_{\text{TA}}(t)$, of MV^{2+} radical generation. Interestingly, as shown in Table 1 and Figure 2C, the average transient quantum yields at 9 – $10 \mu\text{s}$ for NCs closely follow those of steady-state MV^{2+} generation quantum yields. These results suggest that the steady-state quantum yields in these systems are limited by the extent of charge recombination, which is determined by the relative rates of hole filling (τ_{HF}) by the sacrificial electron donor (MPA) vs the charge recombination (τ_{CR}) between the hole in the NC and the electron in MV^{2+} radicals. These rates can also be independently determined.

To measure the charge recombination rate, we investigated NC- MV^{2+} complexes in chloroform in the absence of MPA using TOPO-capped (water insoluble) NCs. As shown in Figure S6 in SI, the MV^{2+} radicals are formed within hundreds of femtoseconds for all NCs except for CdSe/CdS CS-SV (20 ps), similar to MPA-capped NCs in aqueous solution (Figure 4). However, these kinetics show much faster decay of MV^{2+} radicals, reflecting the charge recombination process on the subnanosecond to microsecond time scale. These recombination kinetics traces are non-single-exponential. Therefore, we list the half-life times in Table 1 to approximately represent the charge recombination time (τ_{CR}) in NC- MV^{2+} complexes.

To measure the hole-transfer rate, we investigated MPA-capped NCs in aqueous solutions with excess MPA and without MV^{2+} . Under these conditions, the hole can be removed by trapping within the NC, transferring to MPA, and recombining with the conduction band electron. The dynamics of the conduction band electron can be independently probed by transient bleach kinetics of the exciton bands, as mentioned above, while the fluorescence decay reflects the depopulation of the electron and/or hole. Therefore, hole transfer to MPA and/or trapping increases the NC fluorescence decay rate without affecting the transient bleach recovery kinetics, while exciton (electron-hole) recombination leads to correlated decay of fluorescence and exciton bleach recovery. For CdSe seed, CdSe/CdS CS-SE, and CdSe/CdS DIR, the fluorescence decay is much faster than the transient bleach recovery (Figure S7 in SI), suggesting that holes decay by either trapping or transfer to MPA. Furthermore, TOPO capped NCs (before ligand

exchange by MPA) shows negligible fluorescence decay on the same time scale (Figure S7 in SI), indicating negligible electron or hole trapping in the observed time window. Assuming that ligand exchange from TOPO to MPA does not significantly increase the hole-trapping rates, these results suggest that hole transfer to MPA is the main pathway for the ultrafast emission decay in the MPA–NC complexes. The half lifetimes of these fluorescence decay curves are determined to represent the hole filling time (τ_{HF} , Table 1). For CdSe/CdS CS-SV, the transient bleach recovery and fluorescence decay have the same kinetics (Figure S7D), suggesting that hole filling is much slower than the intrinsic electron–hole recombination. Therefore, the hole filling time is estimated to be $\gg 100$ ns in these giant QDs. For CdS NRs, the holes are trapped within the instrument response time of this measurement and the trapped hole can also be filled by MPA with a half-life of 0.62 ns (Figure S8 in SI). Because of the limited instrument response time of the fluorescence decay measurements, faster decay component (< 100 ps) may be missed and the estimated hole transfer lifetimes in Table 1 should be considered as a upper limit.

Wave Function Engineering in Nanostructures. The results presented here show that the steady-state quantum yields of $\text{MV}^{+\bullet}$ radical generation in NC-based photoreduction systems depend sensitively on the composition and shape of the NCs. In all MPA–NC– MV^{2+} complexes the initial charge separation is 100% because the charge separation rates are much faster than the intrinsic electron–hole recombination rates in all NCs (i.e., $\tau_{\text{CS}} \ll \tau_{\text{RX}}$). However, the charge recombination (τ_{CR}) and hole-filling (τ_{HF}) rates differ in these materials, giving rise to the variation in MV^{2+} photoreduction efficiencies. For CdSe seed, both the charge recombination and the hole filling are fast (Figure 5A), leading to a relatively small yield of radical generation. Coating the CdSe seed by a CdS shell creates quasi-type II core/shell structures in which the electron is delocalized in both the core and shell while the hole is localized in the core.⁴⁹ For CdSe/CdS CS-SE (with a thin CdS shell), the quasi-type II band alignment enables similarly fast charge separation as in CdSe seed while it retards the charge recombination process by 30 times (Figure S6 in SI).^{13,14} For reasons yet to be understood, the hole filling time is only slowed down by a factor 2. One possibility may be the reduction of hole trap states in the CdSe surface with the epitaxially grown CdS shell. Thus, the more competitive hole filling process in these quasi-type II core/shell structures increases the overall yield of $\text{MV}^{+\bullet}$ radical generation. Further growth of a thicker CdS shell in CdSe/CdS SV (radius of ~ 6 nm) reduces the charge separation rate by a factor of ~ 50 due to the reduction of electron density at the QD surface. Efficient charge separation can still be achieved because this separation rate is significantly faster than the single exciton lifetime. However, the thick shell slows down both the charge recombination and hole filling rate, resulting in negligible improvement of the steady-state radical generation yield.

Unlike the spherical CdSe/CdS core/shell QDs, the CdSe/CdS DIR NRs reduce the charge recombination rate without decreasing the hole removal rate (Figure 5B). It has been shown that CdSe/CdS DIR with small CdSe seed forms a quasi-type II structure with the hole confined in CdSe and the electron delocalized in the rod, as indicated in Figure 1B.^{50,51} The delocalized conduction band electron in the rod is quantum-confined in the direction perpendicular to the long axis of the rod, which extends its wave function to the NR surface and facilitates ultrafast electron transfer to MV^{2+} .¹³ The

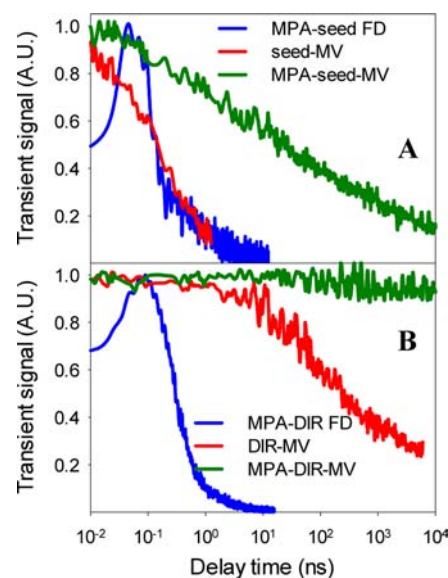


Figure 5. Comparison of hole-filling and charge recombination kinetics in different NCs: (A) CdSe seed and (B) CdSe/CdS DIR. The hole-filling time is measured by fluorescence decay kinetics of MPA–NCs in water (blue line). The charge recombination time is monitored by the $\text{MV}^{+\bullet}$ decay kinetics of NC– MV^{2+} complexes in chloroform (red line). Also shown for comparison is the $\text{MV}^{+\bullet}$ decay kinetics of MPA–NC– MV^{2+} complexes in water (green line). In the presence of MPA, the lifetime of $\text{MV}^{+\bullet}$ becomes longer due to the removal of the hole by MPA. The initial rise of the fluorescence decay curve is due to the slow instrument response time (~ 50 ps) of this measurement.

hole wave function, localized in the CdSe dot, can also extend to the surface in the radial direction, which enables fast hole removal by sacrificial electron donors. Furthermore, the electron and hole are separated along the NR axis, slowing down the electron–hole (τ_{RX}) and charge (τ_{CR}) recombination rates. Thus, these nanorod heterostructures offer the unique ability to vary the composition as well as radial and axial dimensions to simultaneously enhance the rates of forward processes and slow down the rates of backward processes shown in Figure 1.

It is interesting to note that the steady-state $\text{MV}^{+\bullet}$ radical generation yield in CdS NRs is higher than the spherical QDs. A comparison of the transient exciton bleach recovery and fluorescence decay of free CdS NRs (without MV^{2+} or MPA) indicates ultrafast (< 100 ps, instrument-response limited) intrinsic hole trapping in CdS NRs while the conduction band electron is long-lived (see SI 8 in SI). Similar ultrafast hole-trapping processes have also been reported previously in CdS QDs.^{52,53} Thus, in the CdS NRs, the hole is localized in the trap and spatially separated from the electron, similar to the electron and hole distributions in quasi-type II CdSe/CdS NRs. These charge distributions in CdS NRs enable ultrafast interfacial electron transfer and hole filling, and slows down charge recombination, leading to an improved $\text{MV}^{+\bullet}$ radical generation yield compared to spherical QDs. However, the recombination rate is about 15 times faster and the hole-filling rate is about 2 times slower than those of CdSe–CdS DIRs, which may account for the lower overall $\text{MV}^{+\bullet}$ radical generation yield using CdS NRs.

CONCLUSIONS

In conclusion, through controlling the composition, size, and shape of nanoheterostructures, near-unity quantum yield of light-driven methylviologen radical generation has been achieved using colloidal quasi-type II CdSe/CdS dot-in-rod NRs as the light-harvesting and charge separation components and MPA as the sacrificial hole acceptor. The quantum yield remains >90% over a broad MV²⁺ concentration range (0.040–125 mM), due to MV²⁺-NR complex formation. Coupled with Pt nanoparticles, this system can efficiently reduce water to form H₂ using solar energy. Because methylviologen is a common redox mediator for many catalytic reactions, including H₂O and CO₂ reduction, this novel system provides a flexible approach for efficient redox mediator-based solar-to-fuel conversion. Comparison of the steady-state mediator photo-reduction quantum yields and transient kinetics of different nanocrystals suggests that the dot-in-rod nanostructures facilitate interfacial electron transfer to the mediator and interfacial hole transfer to the hole acceptor while simultaneously retarding the charge recombination process. These advantageous properties can be attributed to the electron and hole wave function distributions in this material. Our finding suggests that wave function engineering in quantum-confined nanoheterostructures provides a new avenue for developing novel light-harvesting and charge separation materials for direct solar-to-fuel conversion.

ASSOCIATED CONTENT

Supporting Information

Additional text, figures showing experimental methods, UV–vis spectra of MV²⁺ photoreduction, concentration-dependent kinetics, TA spectra and kinetics in both aqueous solution and chloroform, fluorescence decay kinetics of MPA–NC and comparison with TA results. This material is available free of charge via the Internet at <http://pubs.acs.org>.

AUTHOR INFORMATION

Corresponding Author

tlia@emory.edu

Notes

The authors declare no competing financial interest.

ACKNOWLEDGMENTS

This work was in part supported by Lonza Ltd. (Switzerland) as part of Lonza's LIFT program of long term innovation (to T.L.). C.L.H. was supported by the U.S. Department of Energy Office of Basic Energy Sciences, Solar Photochemistry Program (DE-FG02-07ER-15906). We thank Prof. Stefan Lutz for helpful discussions.

REFERENCES

- (1) Lewis, N. S.; Nocera, D. G. *Proc. Natl. Acad. Sci. U.S.A.* **2006**, *103*, 15729.
- (2) Gur, I.; Fromer, N. A.; Geier, M. L.; Alivisatos, A. P. *Science* **2005**, *310*, 462.
- (3) Nozik, A. J.; Beard, M. C.; Luther, J. M.; Law, M.; Ellingson, R. J.; Johnson, J. C. *Chem. Rev.* **2010**, *110*, 6873.
- (4) Talapin, D. V.; Lee, J.-S.; Kovalenko, M. V.; Shevchenko, E. V. *Chem. Rev.* **2009**, *110*, 389.
- (5) Kiwi, J.; Gratzel, M. *Nature* **1979**, *281*, 657.
- (6) Kalyanasundaram, K. *Coord. Chem. Rev.* **1982**, *46*, 159.
- (7) Darwent, J. R.; Douglas, P.; Harriman, A.; Porter, G.; Richoux, M.-C. *Coord. Chem. Rev.* **1982**, *44*, 83.

- (8) O'Regan, B.; Gratzel, M. *Nature* **1991**, *353*, 737.
- (9) Kamat, P. V.; Tvrđy, K.; Baker, D. R.; Radich, J. G. *Chem. Rev.* **2010**, *110*, 6664.
- (10) Alivisatos, A. P.; Gu, W.; Larabell, C. *Annu. Rev. Biomed. Eng.* **2005**, *7*, 55.
- (11) Wu, X. Y.; Liu, H. J.; Liu, J. Q.; Haley, K. N.; Treadway, J. A.; Larson, J. P.; Ge, N. F.; Peale, F.; Bruchez, M. P. *Nat. Biotechnol.* **2003**, *21*, 41.
- (12) Mirkin, C. A.; Letsinger, R. L.; Mucic, R. C.; Storhoff, J. J. *Nature* **1996**, *382*, 607.
- (13) Zhu, H.; Song, N.; Lian, T. *J. Am. Chem. Soc.* **2010**, *132*, 15038.
- (14) Zhu, H.; Song, N.; Lian, T. *J. Am. Chem. Soc.* **2011**, *133*, 8762.
- (15) Cozzoli, P. D.; Pellegrino, T.; Manna, L. *Chem. Soc. Rev.* **2006**, *35*, 1195.
- (16) Zhu, H.; Song, N.; Rodríguez-Córdoba, W.; Lian, T. *J. Am. Chem. Soc.* **2012**, *134*, 4250.
- (17) Amirav, L.; Alivisatos, A. P. *J. Phys. Chem. Lett.* **2010**, *1*, 1051.
- (18) Tang, M. L.; Grauer, D. C.; Lassalle-Kaiser, B.; Yachandra, V. K.; Amirav, L.; Long, J. R.; Yano, J.; Alivisatos, A. P. *Angew. Chem., Int. Ed.* **2011**, *50*, 10203.
- (19) Gust, D.; Moore, T. A.; Moore, A. L. *Acc. Chem. Res.* **2001**, *34*, 40.
- (20) Holten, D.; Bocian, D. F.; Lindsey, J. S. *Acc. Chem. Res.* **2002**, *35*, 57.
- (21) Magnuson, A.; Anderlund, M.; Johansson, O.; Lindblad, P.; Lomoth, R.; Polivka, T.; Ott, S.; Stensjö, K.; Styring, S.; Sundström, V.; Hammarström, L. *Acc. Chem. Res.* **2009**, *42*, 1899.
- (22) Vignais, P. M.; Billoud, B. *Chem. Rev.* **2007**, *107*, 4206.
- (23) Harriman, A.; Porter, G.; Richoux, M.-C. *J. Chem. Soc., Faraday Trans. 2* **1981**, *77*, 833.
- (24) Brugger, P. A.; Cuendet, P.; Graetzel, M. *J. Am. Chem. Soc.* **1981**, *103*, 2923.
- (25) Peck, H. D.; Gest, H. *J. Bacteriol.* **1956**, *71*, 70.
- (26) Okura, I.; Kim-Thuan, N.; Takeuchi, M. *Angew. Chem., Int. Ed. Engl.* **1982**, *21*, 434.
- (27) Parkinson, B. A.; Weaver, P. F. *Nature* **1984**, *309*, 148.
- (28) Willner, I.; Mandler, D. *J. Am. Chem. Soc.* **1989**, *111*, 1330.
- (29) Willner, I.; Riklin, A.; Lapidot, N. *J. Am. Chem. Soc.* **1990**, *112*, 6438.
- (30) Willner, I.; Lapidot, N.; Riklin, A.; Kasher, R.; Zahavy, E.; Katz, E. *J. Am. Chem. Soc.* **1994**, *116*, 1428.
- (31) Koga, H.; Hamada, T.; Sakaki, S. *Dalton Trans.* **2003**, 1153.
- (32) Burai, T. N.; Panay, A. J.; Zhu, H.; Lian, T.; Lutz, S. *ACS Catalysis* **2012**, 667.
- (33) Morris-Cohen, A. J.; Frederick, M. T.; Cass, L. C.; Weiss, E. A. *J. Am. Chem. Soc.* **2011**, *133*, 10146.
- (34) Matylytsky, V. V.; Dworak, L.; Breus, V. V.; Basche, T.; Wachtveitl, J. *J. Am. Chem. Soc.* **2009**, *131*, 2424.
- (35) Gratzel, M.; Moser, J. *Proc. Natl. Acad. Sci. U.S.A.* **1983**, *80*, 3129.
- (36) Harris, C.; Kamat, P. V. *ACS Nano* **2010**, *4*, 7321.
- (37) Sitt, A.; Sala, F. D.; Menagen, G.; Banin, U. *Nano Lett.* **2009**, *9*, 3470.
- (38) Carbone, L.; Nobile, C.; De Giorgi, M.; Sala, F. D.; Morello, G.; Pompa, P.; Hytch, M.; Snoeck, E.; Fiore, A.; Franchini, I. R.; Nadasan, M.; Silvestre, A. F.; Chiodo, L.; Kudera, S.; Cingolani, R.; Krahne, R.; Manna, L. *Nano Lett.* **2007**, *7*, 2942.
- (39) Yu, W. W.; Qu, L. H.; Guo, W. Z.; Peng, X. G. *Chem. Mater.* **2003**, *15*, 2854.
- (40) Watanabe, T.; Honda, K. *J. Phys. Chem.* **1982**, *86*, 2617.
- (41) Kalyanasundaram, K.; Kiwi, J.; Grätzel, M. *Helv. Chim. Acta* **1978**, *61*, 2720.
- (42) Crutchley, R. J.; Lever, A. B. P. *J. Am. Chem. Soc.* **1980**, *102*, 7128.
- (43) Mandal, K.; Hoffman, M. Z. *J. Phys. Chem.* **1984**, *88*, 5632.
- (44) Harriman, A.; Porter, G. *J. Chem. Soc., Faraday Trans. 2* **1982**, *78*, 1937.
- (45) Kiwi, J.; Graetzel, M. *J. Am. Chem. Soc.* **1979**, *101*, 7214.
- (46) Ebbesen, T. W. *J. Phys. Chem.* **1984**, *88*, 4131.

- (47) Du, P.; Schneider, J.; Jarosz, P.; Eisenberg, R. *J. Am. Chem. Soc.* **2006**, *128*, 7726.
- (48) Aldana, J.; Lavelle, N.; Wang, Y. J.; Peng, X. G. *J. Am. Chem. Soc.* **2005**, *127*, 2496.
- (49) Garcia-Santamaría, F.; Chen, Y.; Vela, J.; Schaller, R. D.; Hollingsworth, J. A.; Klimov, V. I. *Nano Lett.* **2009**, *9*, 3482.
- (50) Luo, Y.; Wang, L.-W. *ACS Nano* **2009**, *4*, 91.
- (51) Rainò, G.; Stöfferle, T.; Moreels, I.; Gomes, R.; Kamal, J. S.; Hens, Z.; Mahrt, R. F. *ACS Nano* **2011**, *5*, 4031.
- (52) Klimov, V.; Bolivar, P. H.; Kurz, H. *Phys. Rev. B* **1996**, *53*, 1463.
- (53) Garrett, M. D.; Dukes Iii, A. D.; McBride, J. R.; Smith, N. J.; Pennycook, S. J.; Rosenthal, S. J. *J. Phys. Chem. C* **2008**, *112*, 12736.